Received: 7 February 2022 | Revised: 1 June 2022 | Accepted: 19 June 2022

DOI: 10.1002/nbm.4790

RESEARCH ARTICLE

NMR IN BIOMEDICINE WILEY

Advanced design of MRI inversion pulses for inhomogeneous field conditions by optimal control

Christina Graf[1] | Martin Soellradl[1] | Christoph Stefan Aigner[2] | Armin Rund[3] | Rudolf Stollberger[1]

[1]Institute of Biomedical Imaging, Graz University of Technology, Graz, Austria

[2]Physikalisch-Technische Bundesanstalt (PTB), Braunschweig and Berlin, Germany

[3]Institute for Mathematics and Scientific Computing, University of Graz, Graz, Austria

Correspondence
Rudolf Stollberger, Institute of Biomedical Imaging, Graz University of Technology, Graz, Austria.
Email: rudolf.stollberger@tugraz.at

Present Address
Stremayrgasse 16/III, 8010 Graz, Austria.

Summary

Non-selective inversion pulses find widespread use in MRI applications, where requirements on them are increasingly demanding. With the use of high and ultra-high field strength systems, robustness to ΔB_0 and B_1^+ inhomogeneities, while tackling SAR and hardware limitations, has rapidly become important. In this work, we propose a time-optimal control framework for the optimization of ΔB_0- and B_1^+-robust inversion pulses. Robustness is addressed by means of ensemble formulations, while allowing inclusion of hardware and energy limitations. The framework is flexible and performs excellently for various optimization goals. The optimization results are analyzed extensively in numerical experiments. Furthermore, they are validated, and compared with adiabatic RF pulses, in various phantom and in vivo measurements on a 3 T MRI system.

KEYWORDS
Inhomogeneous B_0 and B_1, MRI, RF pulse design, time-optimal control

1 | INTRODUCTION

Non-selective inversion pulses have significant impact on image contrast and quantification in various applications such as fluid attenuated inversion recovery (FLAIR),[1] double- or multi-inversion recovery,[2–4] MRS,[5] background suppression in arterial spin labeling (ASL),[6,7] or myocardial T_1 mapping.[8–11] Amplitude-modulated pulses such as block or sinc pulses could be used for inversion; however, they are prone to B_1^+ inhomogeneities and off-resonance effects, which have direct impact on the flip angle and therefore the inversion efficiency. To improve robustness towards inhomogeneities, composite or adiabatic RF pulses[12–15] were explored. However, the extent of robustness amongst B_1^+ and ΔB_0 inhomogeneities is limited using composite pulses.[16] Adiabatic pulses[12,13,15,17,18] exhibit increased robustness, but typically require a prolonged pulse duration and large RF amplitude, leading to a high energy deposition. Moreover, because of shorter T_2 times at higher field strength, relaxation effects for the usual longer adiabatic pulses may have an impact on the pulse performance. Besides, already at 3 T spatially varying B_1^+ variations are in the order of 75% to 115% of the normalized value within the human head.[19] For the human abdomen, the impact on the RF uniformity increases due to the larger body dimension,[20,21] and for higher field strengths because of a shorter wavelength,[22] leaving adiabatic and composite RF pulses with insufficient robustness. Therefore, it would be key to use sufficiently robust, short RF pulses,[12–14,23–29] which fulfill specific absorption rate (SAR) and hardware limitations of the MRI system in addition.

Abbreviations used: ASL, arterial spin labeling; FLAIR, fluid attenuated inversion recovery; FOV, field of view; HS, hyperbolic secant; PI, power intgral; SAR, specific absorption rate; T_E, echo time; T_I, inversion time; T_R, repetition time.

Optimal control plays a growing role in RF pulse design due to its flexibility.[30] Advancements include increasing dimensions,[31] accelerating optimization,[32] or optimization of simultaneous multislice RF pulses with large flip angles and gradient imperfections.[33–36] Robustness amongst B_1^+ inhomogeneities was addressed in different ways, requiring adiabaticity directly,[37] or via an ensemble formulation, i.e., integrating several scales of B_1^+ into the cost functional.[25] The latter was also used[38,39] for the design of preparation pulses for contrast optimization, and for energy efficient excitation pulses, including ΔB_0 robustness.

The aim of this work is the design of ΔB_0- and B_1^+-robust RF pulses with minimal pulse duration that fulfill all given SAR and hardware limitations of the MRI system by optimal control. The cost functional is described by ensemble formulations,[25] with additional time minimization proposed here. Compared with Reference [30], the minimization is done simultaneously for pulse duration and the gap towards the desired magnetization. The optimization method features convergence independent of an educated initial guess, which is demonstrated by using a random initialization. The underlying Bloch equations are solved using a symmetric operator splitting[40] with the optimization goal of designing non-selective, robust inversion pulses in minimal time. Furthermore, RF pulses are optimized for diverse requirements regarding ΔB_0 and B_1^+ robustness, demonstrating the flexibility of the proposed optimization framework. The optimized RF pulses are analyzed extensively in numerical studies, where a numerical comparison to two adiabatic, hyperbolic secant pulses is made. The RF pulses are validated on a 3 T MRI system and compared in various phantom and in vivo measurements. The inversion pulses discussed within this paper are available at https://github.com/GrafChristina/RobustInversion.

2 | THEORY

In the following, an optimization problem for robust design of non-selective inversion in minimal time is introduced.

2.1 | Problem formulation

The governing equations are the Bloch equations with relaxation, but without slice-selection, in the rotating frame of reference. Inhomogeneities of the B_1^+ field are included using constants $c_i \in C \subset \mathbb{R}_+$ as scaling factors. This results in $B_1^+(t) \cdot c_i$, where $C = \{c_i, i = 1, \ldots N_{B_1^+}\}$ is the set of different scales of the nominal amplitude under consideration. Furthermore, a set of ΔB_0 offsets $A = \{\Delta B_{0,j}, j = 1, \ldots N_{\Delta B_0}\} \in \mathbb{R}$ with $\Delta B_{0,j} = B_0 - B_j$ is introduced, where $B_0 = \frac{\omega_0}{\gamma}$ is the nominal field strength with ω_0 being the Larmor frequency, and $B_j = \frac{\omega_j}{\gamma}$, with ω_j being the effective frequency of oscillation. The Bloch equations including above defined parameters c_i and $\Delta B_{0,j}$ are given as

$$\begin{cases} \frac{d\mathrm{M}_{i,j}(t)}{dt} = A_{i,j}(t) \cdot \mathrm{M}_{i,j}(t) + \mathrm{b} \text{ for } t \in (0, T), \\ \mathrm{M}_{i,j}(0) = \mathrm{M}^0 \end{cases} \tag{1}$$

with

$$A_{i,j} = \begin{pmatrix} -\frac{1}{T_2} & \gamma \Delta B_{0,j} & -\gamma B_{1,y}^+(t) \cdot c_i \\ -\gamma \Delta B_{0,j} & -\frac{1}{T_2} & \gamma B_{1,x}^+(t) \cdot c_i \\ \gamma B_{1,y}^+(t) \cdot c_i & -\gamma B_{1,x}^+(t) \cdot c_i & -\frac{1}{T_1} \end{pmatrix} \tag{2}$$

and

$$b = \begin{pmatrix} 0 \\ 0 \\ \frac{M_0}{T_1} \end{pmatrix}. \tag{3}$$

Note that $A_{i,j}$ is the Bloch matrix for a certain B_1^+ scaling c_i and a certain offset $\Delta B_{0,j}$. $B_1^+(t) = B_{1,x}^+(t) + iB_{1,y}^+(t)$ is the complex RF pulse, T_1 and T_2 are the longitudinal and transverse relaxation times, γ is the gyromagnetic ratio, and $\mathrm{M}^0 \in \mathbb{R}^3$ the initial magnetization. Moreover, $M_0 = |\mathrm{M}^0|$ is the equilibrium magnetization and T is the terminal time or pulse duration.

Here, a robust optimization problem for RF pulse design is introduced. The goal is to design an RF pulse that drives the magnetization $\mathrm{M}(T)$ at the terminal time T close to a desired magnetization $\mathrm{M}_{\mathrm{des}}$ robustly for all included combinations of B_1^+ inhomogeneities and ΔB_0 offsets. This is modeled as

$$\left|\mathrm{M}_{i,j}(T) - \mathrm{M}_{\mathrm{des}}\right| \leq \varepsilon \tag{4}$$

with ε being the maximal gap between actual magnetization and desired magnetization. The RF pulse $B_1^+(t)$ is optimized using polar coordinates $(r(t), \varphi(t))$ with $r(t) = \left|B_1^+(t)\right|$ and $\varphi(t) = \mathrm{angle}(B_1^+(t))$ with given bounds

$$0 \leq r(t) \leq r_{\max},\ 0 \leq \varphi(t) < 2\pi \ \ \forall t \in (0, T). \tag{5}$$

The ΔB_0- and B_1^+-robust optimal control problem for best approximation in minimum time is then given as

$$\begin{cases} \min\limits_{T>0,\, r,\, \varphi} J = T + \dfrac{\alpha}{2}\displaystyle\int_0^T \varphi(t)^2 dt + \dfrac{\alpha}{2}\int_0^T r(t)^2 dt, \\ \text{subject to } (1),\ (4) \text{ and } (5),\ \text{for all } i \text{ and } j. \end{cases} \tag{6}$$

The cost functional also features a pulse energy term with cost parameter $\alpha > 0$.

2.2 | Optimal control theory

For reasons of numerical optimal control (improve convergence and globalization as state-constrained problems typically show worse characteristics here), the state constraints (4) are replaced by an L^p- penalization term following Reference [34]. With $p \in \mathbb{N}$, p even, the optimal control problem transforms into

$$\begin{cases} \min\limits_{T>0,\, r,\, \varphi} J_{\mathrm{pen}} = J + \dfrac{\mu}{p}\displaystyle\sum_{i=1}^{N_{B_1^+}}\sum_{j=1}^{N_{\Delta B_0}} \left(\frac{\mathrm{M}_{i,j}(T) - \mathrm{M}_{\mathrm{des}}}{\varepsilon}\right)^p \\ \text{subject to } (1) \text{ and } (5). \end{cases} \tag{7}$$

Herein, $\mu > 0$ is a penalization parameter. For performance reasons, derivative-based optimal control methods are applied. The gradient of the cost functional can be computed in high precision via solving adjoint equations (compare Reference[41]). The adjoint equations of the robust optimal control problem for a certain B_1^+ inhomogeneity c_i and an offset $\Delta B_{0,j}$ are given as

$$\begin{cases} -\dfrac{d\mathrm{q}_{i,j}(t)}{dt} = A_{i,j}(t)^{\mathsf{T}} \cdot \mathrm{q}_{i,j}(t) \ \text{ in } (0, T), \\ \mathrm{q}_{i,j}(T) = \left(0, 0, \frac{\mu}{\varepsilon^p}\left(\frac{\mathrm{M}_{i,j}(T) - \mathrm{M}_{\mathrm{des}}}{\varepsilon}\right)^{p-1}\right)^{\mathsf{T}}. \end{cases} \tag{8}$$

Herein, $A_{i,j}$ is the Bloch matrix. Note that the equation is computed backwards in time. With the control in Cartesian coordinates $(B_{1,x}^+, B_{1,y}^+)$, the reduced gradient of the cost functional is given as

$$\mathrm{g}\left(B_{1,x}^+, B_{1,y}^+\right) = \begin{pmatrix} \mathrm{g}_1 \\ \mathrm{g}_2 \end{pmatrix} = \begin{pmatrix} \alpha B_{1,x}^+ + \displaystyle\sum_{i=1}^{N_{B_1^+}}\sum_{j=1}^{N_{\Delta B_0}} \mathrm{q}_{i,j}^{\mathsf{T}} A_{1,i,j} \mathrm{M}_{i,j} \\ \alpha B_{1,y}^+ + \displaystyle\sum_{i=1}^{N_{B_1^+}}\sum_{j=1}^{N_{\Delta B_0}} \mathrm{q}_{i,j}^{\mathsf{T}} A_{2,i,j} \mathrm{M}_{i,j} \end{pmatrix},$$

where

$$A_{1,ij} = \begin{pmatrix} 0 & 0 & 0 \\ 0 & 0 & \gamma \cdot c_i \\ 0 & -\gamma \cdot c_i & 0 \end{pmatrix},$$
$$A_{2,ij} = \begin{pmatrix} 0 & 0 & -\gamma \cdot c_i \\ 0 & 0 & 0 \\ \gamma \cdot c_i & 0 & 0 \end{pmatrix}$$

are submatrices of the Bloch matrix $A_{i,j}$. In polar coordinates, the reduced gradient is given as

$$\hat{g}(r,\varphi) = \begin{pmatrix} g_1 \sin(\varphi) + g_2 \cos(\varphi) \\ -g_1 r \cos(\varphi) + g_2 r \sin(\varphi) \end{pmatrix}, \tag{9}$$

which is the basis for the following numerical optimization.

For a numerical solution of the Bloch equations as well as for optimization, a piecewise constant discretization of the temporal domain is introduced. The temporal domain $[0, T]$ is discretized into $0 = t_0 < t_1 < \ldots t_{N_u} = T$ with a constant time step length $\Delta t = t_m - t_{m-1}$. Now, applying this discretization to Equation (1) results in piecewise constant Bloch matrices $A_{m,i,j} = A(t_m, c_i, \Delta B_{0,j})$ and a magnetization vector $M_{i,j}(t_m) = M_{c_i,\Delta B_{0,j}}(t_m)$. The discretized Bloch equations are then solved numerically using a symmetric operator splitting scheme, allowing for a fast and accurate solution with included relaxation effects.[40]

Accordingly, the adjoint Equations (8), the reduced numerical gradient of the cost functional (9), as well as the cost functional itself (7) can be expressed by means of the above described discretization. This results in the cost

$$J_\Delta = T + \frac{\alpha}{2}\sum_{k=0}^{N_u} r_k^2 + \frac{\alpha}{2}\sum_{k=0}^{N_u} \varphi_k^2 + \frac{\mu}{p}\sum_{i=1}^{N_{B_1^+}}\sum_{j=1}^{N_{\Delta B_0}} \left(\frac{M_{i,j}(T) - M_{des}}{\varepsilon}\right)^p. \tag{10}$$

3 | METHODS

3.1 | Optimization

The proposed cost functional (10) as well as the calculation of its numerical gradient was implemented in MATLAB (MathWorks, Natick, MA, USA, Release 2017b). The optimization itself was based on a trust-region, semi-smooth quasi-Newton method.[42]

The aim of the optimization was a non-selective, robust inversion pulse, so the desired state for optimization was chosen as $M_{des} = (0, 0, -1)^T$. B_1^+ robustness was desired for a scale of the nominal amplitude of 70% to 130% with $N_{B_1^+} = 7$ steps, so $c_1 = 70\%, \ldots c_7 = 130\%$. Simultaneously, ΔB_0 robustness was desired for an offset of ± 5ppm in $N_{\Delta B_0} = 11$ steps, therefore $\Delta B_{0,1} = -5$ppm, $\ldots \Delta B_{0,11} = +5$ppm. The maximum allowed gap to the desired magnetization was set to $\varepsilon = 0.07$, being equal to a desired inversion efficiency of at least 93%. The parameters are set to $\mu = 1 \times 10^4$, $\alpha = 1$, and α is balanced relative to μ every 200 iterations based on

$$\alpha = \alpha \min\left(2, \max\left(\frac{1}{2}, 2 - 1 \cdot \frac{\gamma_1}{\gamma_2}\right)\right), \quad \gamma_1 = \max_{i,j} |M_{i,j}(T) - M_{des}|/\varepsilon, \quad \gamma_2 = \sum_{k=0}^{N_u} r_k^2 / S, \tag{11}$$

with $S = 0.1$. Herein, γ_1 and γ_2 measure the current state of the desired magnetization and the pulse energy.

The proposed optimization method designs pulses independent of a sophisticated initial guess due to a globalization by a trust-region framework.[42] For demonstration, a pulse with a duration of 10ms and a constant time step length of $\Delta t = 0.01$ms with a random magnitude and phase was used as initial RF pulse for optimization. Corresponding to the T_1 and T_2 values of our cylindrical MR phantom, we set the relaxation times to $T_1 = 102$ms and $T_2 = 81$ms at 3 T during optimization. The box constraints were set to $r_{max} = 20\mu$T to match the amplitude limits of a typical high-end 3 T MRI system.

3.2 | Numerical evaluation

The optimized pulse (optim) was investigated in numerical experiments by comparing it with two adiabatic, hyperbolic secant pulses. The first pulse is defined by a pulse duration of 15.36ms, a bandwidth of $\Delta f = 3.4$kHz and the parameter $\beta = 763$ (HS1); see Figure 1, top. This pulse is commonly used in arterial spin labeling applications.[43] The second pulse (HS2), Figure 1, middle, was designed as a hyperbolic secant pulse as well with an identical pulse duration to the optimized pulse (duration 3.25ms, bandwidth $\Delta f = 1.3$kHz, parameter $\beta = 1374$).

The assessment of the performance of all three pulses was made by calculating the inversion efficiency for all offsets ΔB_0 and all scalings of B_1^+. We analyze the worst case E_{worst}, the best case E_{best} and the median E_{median} defined via

$$E_{\text{worst}} = 1 - \max_{\substack{i=1,\dots N_{B_1^+} \\ j=1,\dots N_{\Delta B_0}}} \left| M_{c_i,\Delta B_{0j}}(T) - (-1) \right|,$$

$$E_{\text{best}} = 1 - \min_{\substack{i=1,\dots N_{B_1^+} \\ j=1,\dots N_{\Delta B_0}}} \left| M_{c_i,\Delta B_{0j}}(T) - (-1) \right|, \tag{12}$$

$$E_{\text{median}} = 1 - \operatorname{median}_{\substack{i=1,\dots N_{B_1^+} \\ j=1,\dots N_{\Delta B_0}}} \left| M_{c_i,\Delta B_{0j}}(T) - (-1) \right|.$$

Furthermore, we depict the range where 90% of the single efficiencies lie, i.e., between 5% and 95% of a histogram distribution. Additionally, the numerical comparison was made not only with relaxation times chosen within the optimization, but also with relaxation times from white matter ($T_1 = 832$ms and $T_2 = 80$ms),[44] and with neglected relaxation effects.

3.3 | Flexibility of the optimization framework

To test the flexibility of the proposed optimization framework with respect to varying optimization targets, four different RF pulses were optimized in addition to the one optimized with parameters as described in Section 3.1 (optim). The first (optim B_1^+) aimed for B_1^+ robustness for a scale of 70% to 130%, but no ΔB_0 robustness. The second pulse (optim ΔB_0) aimed for the opposite, i.e., no B_1^+ robustness, but ΔB_0 robustness for ± 5ppm. The third (optim non-robust) did not include any robustness in the optimization. Finally, optim B_1^+ shift aimed for B_1^+ robustness for

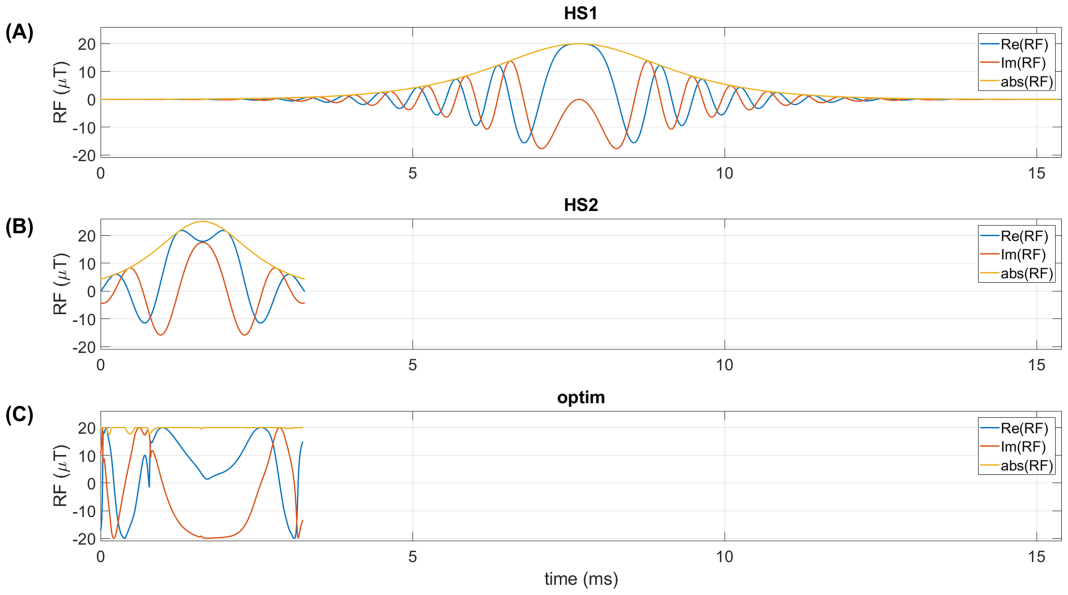

FIGURE 1 Adiabatic RF pulses HS1 (A) and HS2 (B), and optimized RF pulse optim (C). HS1 has a pulse duration of $T = 15.36$ms and a bandwidth of $\Delta f = 3.4$kHz. The other two pulses have a duration of $T = 3.25$ms and bandwidths of $\Delta f = 1.3$kHz and $\Delta f = 2.4$kHz, respectively

70% to 130% and included a single ΔB_0 offset at 3.4ppm to test the influence of a shift of ΔB_0 on the optimization framework, but none at 0ppm. These pulses were evaluated in simulations.

3.4 | Evaluation on the MR scanner

We implemented the optimized RF pulse optim and the two hyperbolic secant pulses HS1 and HS2 on a 3 T MR system (Siemens Magnetom Vida, Siemens Healthcare, Erlangen, Germany) as preparation pulses in a 2D spoiled gradient-echo sequence. Immediately after the preparation pulse and prior to the imaging sequence, a spoiler was added. We used a Siemens 18 channel knee coil for transmit and receive using 1 transmit channel and 18 receive channels.

3.4.1 | Phantom measurements

Extensive experiments to investigate the performance for ΔB_0 and B_1^+ variations were carried out with the cylindrical MR phantom (plastic bottle with diameter 14*cm*, length 42.5*cm*, filled with water containing nickel sulfate, $T_1 = 102$ms and $T_2 = 81$ms). Three different sequences were generated with three different inversion pulses with the following parameters: flip angle $\alpha = 90^\circ$ for the excitation pulse, echo time $T_E = 2.7$ms, inversion time $T_I = 4.5$ms, repetition time $T_R = 700$ms, field of view $(\mathrm{FOV}) = 196\mathrm{mm} \times 159.2\mathrm{mm}$ and $matrix = 128 \times 104$. The flip angles of the inversion pulses were $\beta_{\mathrm{optim}} = 987^\circ, \beta_{\mathrm{HS1}} = 1120^\circ$ and $\beta_{\mathrm{HS2}} = 717^\circ$ (i.e., corresponding to a B_1^+ scale of 100%). To evaluate the robustness of the proposed RF pulses for changes within the nominal B_1^+ field, we changed the transmitter voltage of the inversion pulses $\beta_{\mathrm{optim}}, \beta_{\mathrm{HS1}}$ and β_{HS2} manually on the MR scanner to implicitly induce variations within the amplitude, while the flip angle α of the excitation pulse remained unchanged. For evaluation of robustness with respect to changes in the B_0 field, the carrier frequency of the inversion pulse was shifted manually, which is equivalent to a ΔB_0 shift. Furthermore, we acquired a B_1^+ map using a Bloch–Siegert framework.[45] Here, we set $T_E = 14$ms, $T_R = 122$ms and the parameters regarding geometry as above. For the ΔB_0 map, we used the same geometry and a repetition time of $T_R = 100$ms, and we acquired six echoes within a bipolar acquisition. The odd echoes at $T_E = 2.7, 7.0, 11.4$ms were chosen for the reconstruction of the map. We used both maps to collect regions with the same amplitude and offsets, and their respective inversion efficiencies. Within all measurements, a transversal slice was acquired.

Because of longitudinal relaxation in time between inversion pulse and the excitation pulse, the measured signal is corrected for relaxation effects via

$$M_{z,\mathrm{corr}} = -\sin(\alpha) M_z e^{-T_E/T_2} / (1 - 2e^{-T_I/T_1}). \tag{13}$$

The phantom measurements were made with the three RF pulses optim, HS1 and HS2 with $\Delta B_0 = -7, -5, -3, -1, 0, 1, 3, 5, 7$ppm and a B_1^+ scaling of $0, 20, 40, 60, 80, 100, 120, 140\%$, and all combinations of these. Due to the higher initial RF amplitude of HS2 compared with HS1 and optim, the measurement with a B_1^+ scale of 140% was not possible due to the maximum allowed RF amplitude provided by the transmitter.

3.4.2 | In vivo measurements

MRI was performed after written informed consent in a healthy volunteer. The study was approved by the local ethics committee. The three RF pulses optim, HS1 and HS2 were compared in measurements in a sagittal slice of the volunteer's knee. The sequence parameters were set to $T_E/T_I = 2.7/4.5$ms, $T_R = 6000$ms, FOVread $= 320\mathrm{mm} \times 160\mathrm{mm}$ and matrix $= 288 \times 144$. This experiment was performed for a fixed ΔB_0 offset of 0ppm, and for a B_1^+ scaling of 0% (for inversion efficiency) and 100%. Here, we used a fast Bloch–Siegert approach to acquire a B_1^+ map.[21] The sequence parameters were set to $T_E/T_R = 14.8/90$ms and the geometry was set to values as above. For the measurement of the ΔB_0 map, we used $T_R = 100$ms and we acquired two echoes at $T_E = 4.92, 7.38$ms within a monopolar acquisition.

4 | RESULTS

4.1 | Optimization result and numerical comparison

Figure 1 compares the hyperbolic secant pulses (Figure 1A, HS1; B, HS2) with the optimized RF pulse (Figure 1C, optim). The pulse duration of optim was reduced from an initial value of 10ms to 3.25ms by time-optimal control. The resulting optimized amplitude of the RF pulse (yellow line

in Figure 1) matches the upper box constraint at 20μT for nearly every time point. In addition to Figure 1, Table 1 depicts a numerical comparison between the three RF pulses. We observe a longer pulse duration of HS1 paired with a worse inversion efficiency of the examples considering relaxation effects. HS2 and optim have shorter pulse durations and better inversion efficiencies than HS1, where the efficiency of optim is the best through all sets of relaxation times. The influence of the field inhomogeneities and the possible compensation with the inversion pulses is best seen for E_{worst} and the case without relaxation. With E_{worst} of 85.8% (HS1) and 89.9% (HS2) these pulses are clearly inferior to optim with 96.3%. Note that the areas where the efficiencies were calculated is indicated within Figure 2 (red boxes, i.e., $\Delta B_0 = \pm 5$ppm and B_1^+ scaled for $\pm 30\%$). The bandwidth of HS1 is larger compared with HS2 and optim. The peak B_1^+ amplitudes of HS1 and optim are the same, while that of HS2 is 25% higher. Furthermore, the power integrals of HS1 and HS2 are similar, and that of optim is slightly higher.

Figure 2 illustrates the inversion efficiencies of all three RF pulses as a function of the ΔB_0 offsets and B_1^+ scales for phantom relaxation times. HS1 shows an evenly distributed inversion efficiency for all values of ΔB_0; however, the general efficiency itself is not so good, as indicated by the top plot. In contrast, HS2 shows a better efficiency for smaller offsets of ΔB_0 and small scalings of B_1^+. For a higher offset of ΔB_0, i.e., more than ± 3ppm, the efficiency is below 93% for a B_1^+ scale of 100% and below 90% for a B_1^+ scale of 120%. In contrast, optim shows a very good efficiency, ranging from 94.7% to 97.9% within the red box for which it was optimized. However, also for a higher B_1^+ scaling of 130% to 160%, which

TABLE 1 Numerical comparison between the two hyperbolic secant pulses HS1 and HS2 and the optimized RF pulse optim.

Pulse	T	Δf	Peak B_1^+	PI	E_{worst}	E_{best}	E_{median}	90% range	Relaxation
					71.1	85.94	84.28	[74.71, 85.67]	phantom
HS1	15.36	3.4	20	9.6×10^{-4}	82.8	96.35	95.90	[85.88, 96.33]	white matter
					85.6	99.99	99.31	[88.73, 99.99]	no relax
					85.8	96.75	92.19	[88.29, 96.12]	phantom
HS2	3.25	1.3	25	9.6×10^{-4}	87.8	98.38	93.96	[90.01, 97.92]	white matter
					89.8	99.99	95.59	[91.82, 99.57]	no relax
					94.5	97.92	95.98	[95.33, 97.12]	phantom
optim	3.25	2.5	20	9.6×10^{-4}	94.8	98.18	97.08	[96.01, 97.55]	white matter
					96.3	99.99	99.67	[98.19, 99.98]	no relax

Note: The first four columns show the pulse duration T in ms, the bandwidth of the pulse Δf in kHz, the peak B_1^+ amplitude in μT and the power integral (PI). The last five columns show the inversion efficiency E in % for the specific set of relaxation times over all combinations of ΔB_0 and B_1^+ included in the optimization of optim, i.e., $\Delta B_0 = \pm 5$ppm and B_1^+ scaled for $\pm 30\%$. We depict the worst case, the best case, the median and the range where 90% of the efficiencies lie.

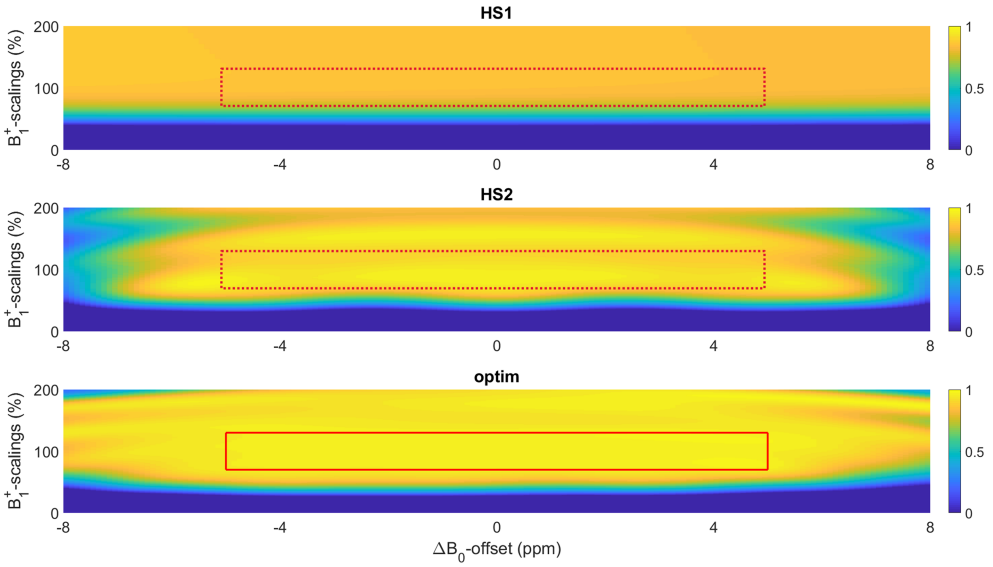

FIGURE 2 Inversion efficiencies for all three RF pulses over all combinations of B_1^+ scalings and ΔB_0 offsets, calculated with the relaxation times from the phantom ($T_1 = 102$ms, $T_2 = 81$ms). The red box indicates the area where the pulse was optimized. The plot shows an efficiency scale from 0 to 1

is outside the optimized box, the efficiency is still good, 93% to 96%. Only at the top corners (high offset of more than $\Delta B_0 = \pm 7$ppm and large B_1^+ scaling of more than 180%) the efficiency is getting worse again, 87% or less.

Figure 3 illustrates RF pulses optimized for specific requirements to illustrate versatility of the implemented method. We observe a further decrease in pulse duration compared with optim. With optim B_1^+ (B_1^+ robust), the pulse duration was reduced from an initial value of 10ms to 1.52ms, where the inversion efficiency for phantom relaxation times is between $E_{worst} = 97.86\%$ and $E_{best} = 98.36\%$ for all included B_1^+ scalings. The pulse duration of optim ΔB_0 (ΔB_0 robust) is similar, 1.56ms, but the efficiency is slightly decreased, $E_{worst} = 96.88\%$ to $E_{best} = 97.92\%$. optim non-robust (assuming ideal ΔB_0 and B_1^+) possesses the shortest duration, 0.58ms, and an efficiency of $E = 99.35\%$ (only one evaluation point here). Finally, the pulse duration of optim B_1^+ shift (B_1^+ robust at $\Delta B_0 = 3.4$ppm) was reduced to 1.49ms, resulting in an inversion efficiency of $E_{worst} = 97.89\%$ to $E_{best} = 98.35\%$.

Similarly to Figure 2, we depict the inversion efficiencies for various combinations of ΔB_0 and B_1^+ in Figure 4. optim B_1^+ (Figure 4A) displays an excellent efficiency for B_1^+ scaled from 70% to more than 150% and no ΔB_0 offset. For B_1^+ at around 65%, inversion is also depicted for ± 6.5ppm. The efficiency for optim ΔB_0 is depicted in Figure 4B. We observe an efficiency of more than 96.5% for ΔB_0 from -5ppm to 5ppm and no scale of B_1^+, i.e., $B_1^+ = 100\%$. optim non-robust (Figure 4C) clearly depicts inversion only for the single point optimized and a little around it. Finally, the efficiency map for optim B_1^+ shift (Figure 4D) looks similar to that of optim B_1^+, but shifted to the right by 3.4ppm.

4.2 | Phantom measurements

Figures 5A, 6A and 7A compare the simulated and the measured inversion efficiencies for all three RF pulses, optim, HS1 and HS2. All plots show a very strong accordance between numerical and measured results. In Figure 5A (optim), we observe that the measured efficiency (bottom line) has values of 94.8% to 97.3% within the area where the red box is. Furthermore, the transition areas from no inversion to inversion look the same, and the off-resonance behaviors within measurements and simulations also show strong agreement. In Figure 5B, the inversion efficiencies on two distinct lines are depicted. Again, within the red boxes, the plots show an evenly distributed inversion efficiency.

Figure 6A (HS1) confirms the efficiency results from numerical simulations within the measurements. As within the simulations (top) we observe a very strong ΔB_0 robustness within the measurements (bottom). Regarding B_1^+, again, we see that for B_1^+ of 90% and more we reach an efficiency of around 85% throughout the plot. Both observations are confirmed by the lineplots in Figure 6B. Finally, in Figure 7A (HS2), we see that for the measurement the efficiency is also very good in the center of the plot (around 96%) and slightly worse to the left and right (around 90% here). Again, the general agreement between simulations and measurements is very strong. Furthermore, in Figure 7B, we recognize the non-even inversion efficiency for changes within B_1^+ (top) as well as ΔB_0 (bottom).

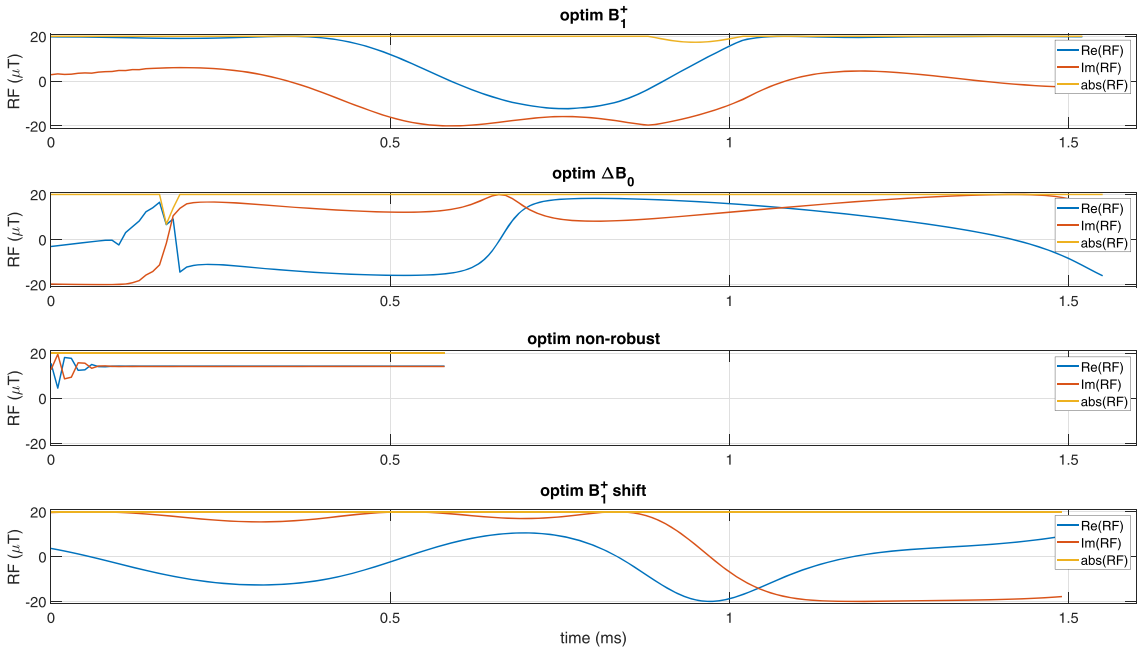

FIGURE 3 Additional pulses optimized for testing the framework. optim B_1^+ aims for B_1^+ robustness only, optim ΔB_0 for ΔB_0 robustness only, optim non-robust for no robustness and optim B_1^+ shift for B_1^+ robustness at $\Delta B_0 = 3.4$ppm

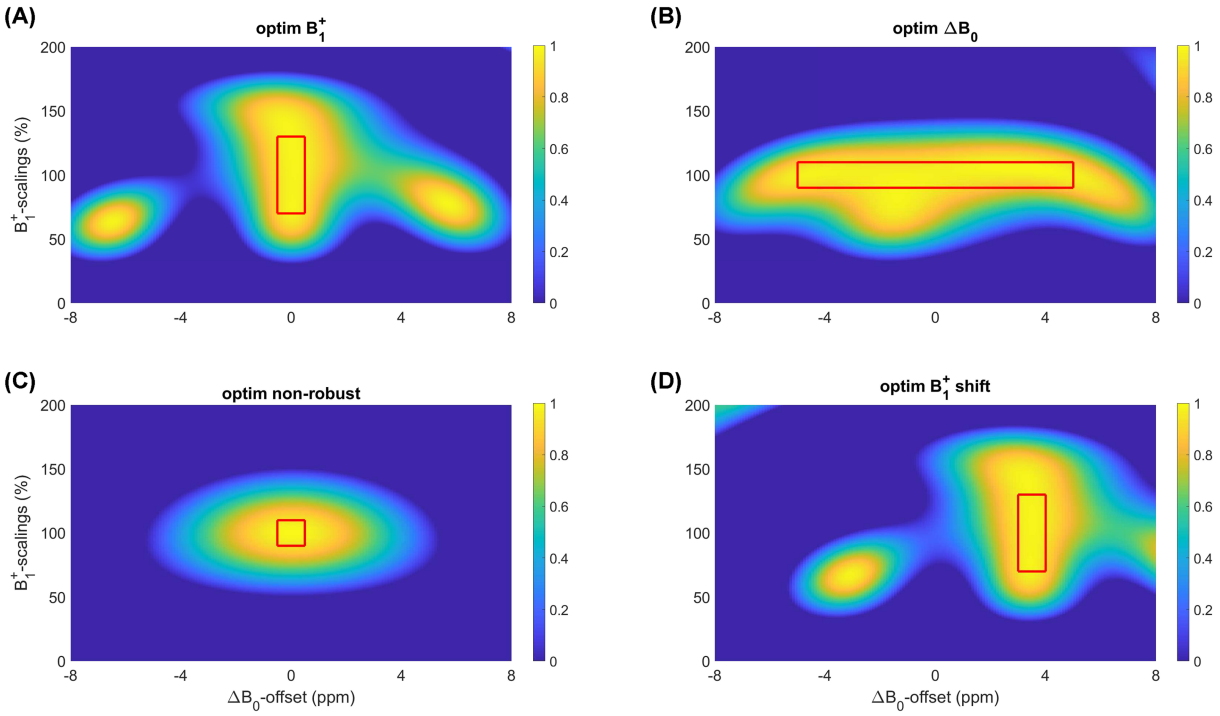

FIGURE 4 Inversion efficiencies for four additional RF pulses, optim B_1^+, optim ΔB_0, optim non-robust and optim B_1^+ shift, for various combinations of B_1^+ scalings and ΔB_0 offsets calculated with the relaxation times from the phantom $T_1 = 102$ms, $T_2 = 81$ms. The plot shows an efficiency scale from 0 to 1. The red boxes indicate the optimization areas

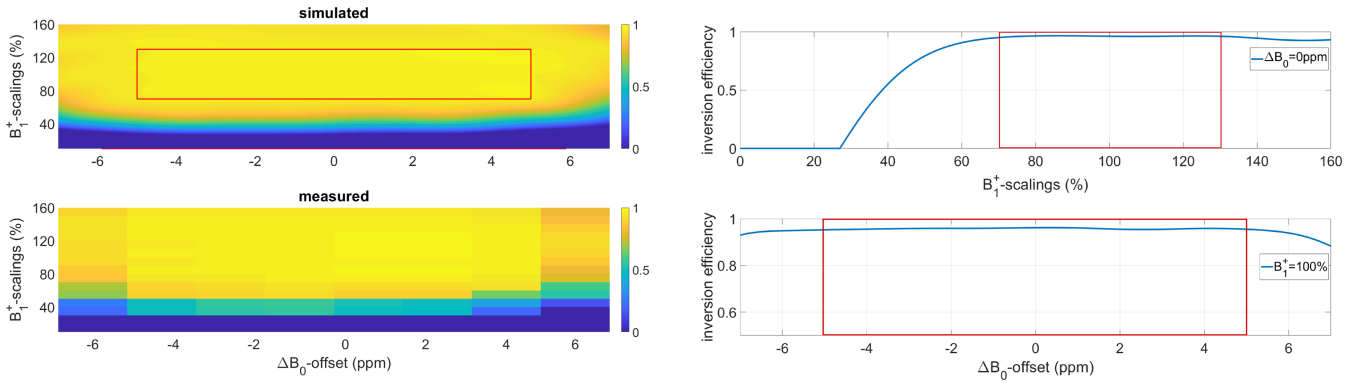

(A) Inversion efficiencies for a broad range of B_1^+ and ΔB_0 values.

(B) Inversion efficiencies on 2 distinct lines.

FIGURE 5 A, Simulated (top) and measured (bottom) inversion efficiencies with optim. B_1^+ is scaled from 0% to 160% and ΔB_0 is included for -7ppm to 7ppm at 3 T. The MR measurements were made with a cylindrical phantom (same relaxation times as in the simulations); the red box indicates the area in which optimization was carried out. B, Simulated inversion efficiencies for a fixed value of $\Delta B_0 = 0$ppm and B_1^+ scaled from 0% to 160% (top) and a fixed B_1^+ scale of 100% and ΔB_0 for -7ppm to 7ppm at 3 T (bottom). Again, the red box depicts the optimized areas. All four plots contain an efficiency scale from 0 to 1

4.3 | In vivo measurements

Figure 8 depicts the inversion efficiencies of the knee measurements for all three RF pulses. Among these three, optim depicts the best inversion performance with the best efficiency towards the proximal and distal directions of the knee. In contrast, HS1 has a decreased efficiency towards the proximal and distal directions. Also in the center, the efficiency is not as good as with optim, 85% to 90%, compared with 90% to 96%. HS2 shows an average performance with an efficiency between those of optim and HS1. Also, towards the proximal and distal directions of the knee, efficiency does not decrease as severely as with HS1. This is especially visible in the line plot at the bottom of the figure. Note that the underlying magnetizations used to calculate this plot were not corrected for relaxation effects.

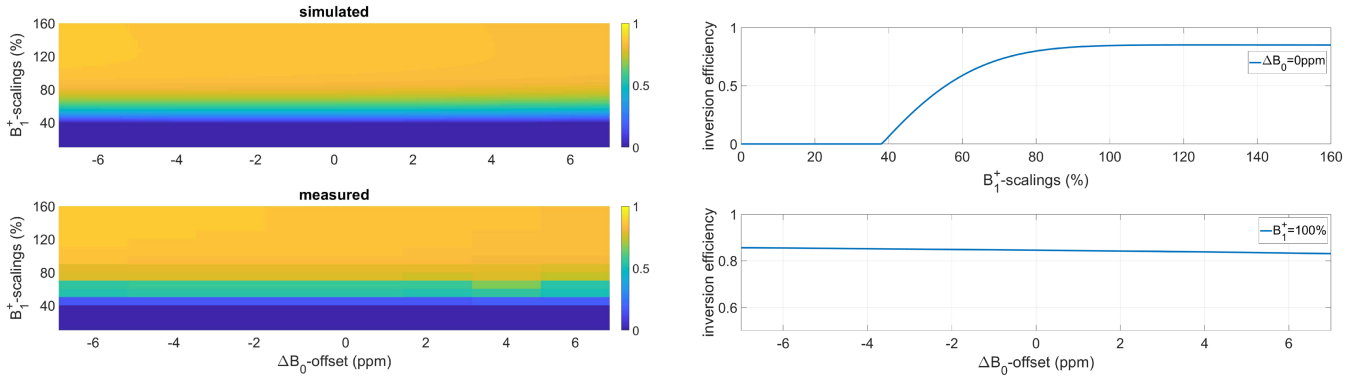

(A) Inversion efficiencies for a broad range of B_1^+ and ΔB_0 values.

(B) Inversion efficiencies on 2 distinct lines.

FIGURE 6 A, Simulated (top) and measured (bottom) inversion efficiencies with HS1. B_1^+ is scaled from 0% to 160% and ΔB_0 is included for −7ppm to 7ppm at 3 T. The MR measurements were made with a cylindrical phantom (same relaxation times as in the simulations). B, Simulated inversion efficiencies for a fixed value of $\Delta B_0 = 0$ppm and B_1^+ scaled from 0% to 160% (top) and a fixed B_1^+ scale of 100% and ΔB_0 for −7ppm to 7ppm at 3 T (bottom). All four plots contain an efficiency scale from 0 to 1

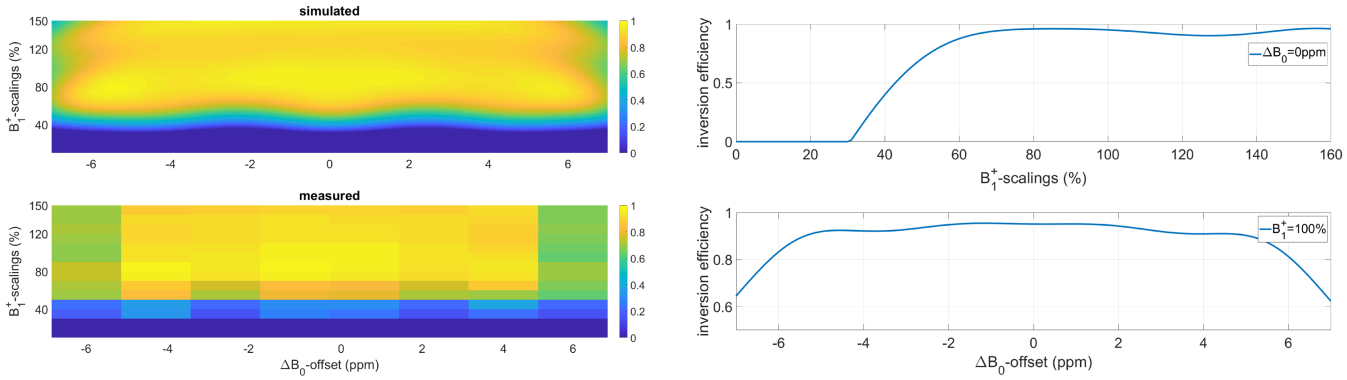

(A) Inversion efficiencies for a broad range of B_1^+ and ΔB_0 values.

(B) Inversion efficiencies on 2 distinct lines.

FIGURE 7 A, Simulated (top) and measured (bottom) inversion efficiencies with HS2. B_1^+ is scaled from 0% to 160% and ΔB_0 is included for −7ppm to 7ppm at 3 T. The MR measurements were made with a cylindrical phantom (same relaxation times as in the simulations). B, Simulated inversion efficiencies for a fixed value of $\Delta B_0 = 0$ppm and B_1^+ scaled from 0% to 160% (top) and a fixed B_1^+ scale of 100% and ΔB_0 for −7ppm to 7ppm at 3 T (bottom). All four plots contain an efficiency scale from 0 to 1

Figure 9A depicts the measured B_0 map of the knee. Deviations within the ΔB_0 field are non-negligible, with values up to ±2.5ppm towards the distal and proximal directions of the knee. Figure 9B illustrates the corresponding B_1^+ map of the knee (with a targeted amplitude of $B_1^+ =$ 9.46μT here). We observe a drop in amplitude in the distal and the proximal directions of the knee, while in the center B_1^+ is considerably homogeneous.

5 | DISCUSSION

ΔB_0- and B_1^+-robust, non-selective inversion pulses with increased inversion efficiency compared with state-of-the-art adiabatic RF pulses were designed by use of time-optimal control techniques. The cost functional allows not only the optimization of the inversion pulse, but also the consideration of various constraints for the practical implementation. Here, the requirement for ΔB_0 and B_1^+ robustness was fulfilled using an ensemble formalization, i.e., including all offsets of ΔB_0 and all scalings of B_1^+ in the cost functional so that a minimum gap to a desired magnetization was reached for each pair. Furthermore, minimization of this gap (which corresponds directly to maximization of inversion efficiency) was conducted. Compared with Reference [37], where robustness was required in terms of adiabaticity, this is a fundamentally different approach, yielding a wider solution space. For implementation on a clinical scanner, hardware limitations and limitations on the pulse energy were met using box constraints and a L^2 regularization of the RF. Regarding the effort of the optimization, the computational time scales quadratically in the number of

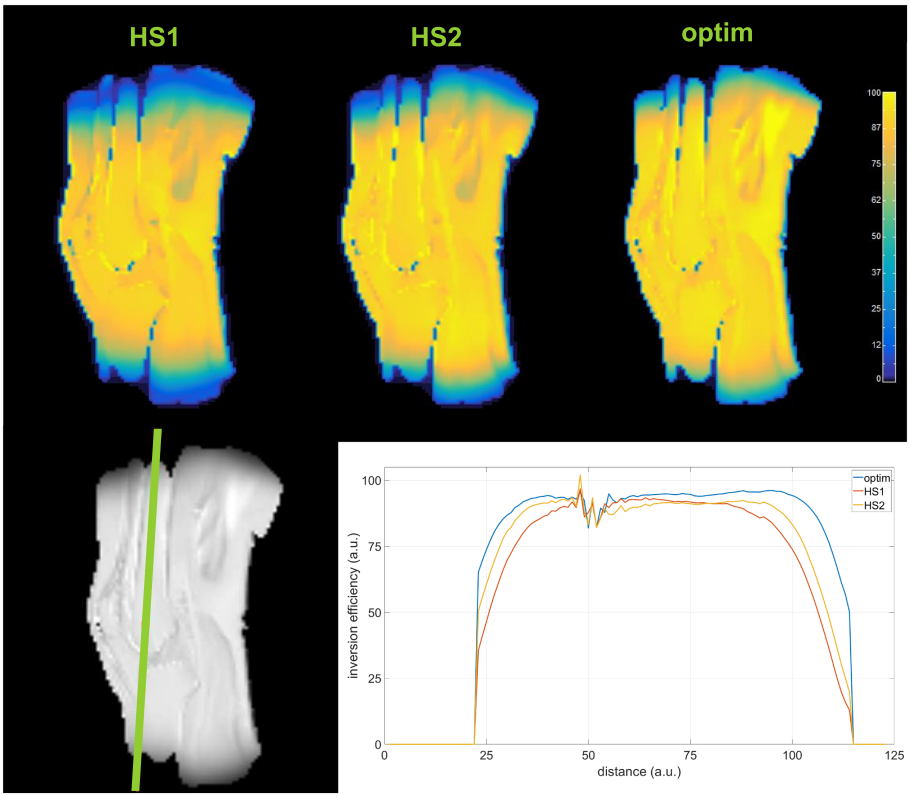

FIGURE 8 Top, Inversion efficiency plots for optim, HS1 and HS2 of a sagittal slice of the knee. The plot depicts an efficiency scale of 0% to 105%. Bottom, Inversion profile on a distinct line (defined left) for all pulses on the right

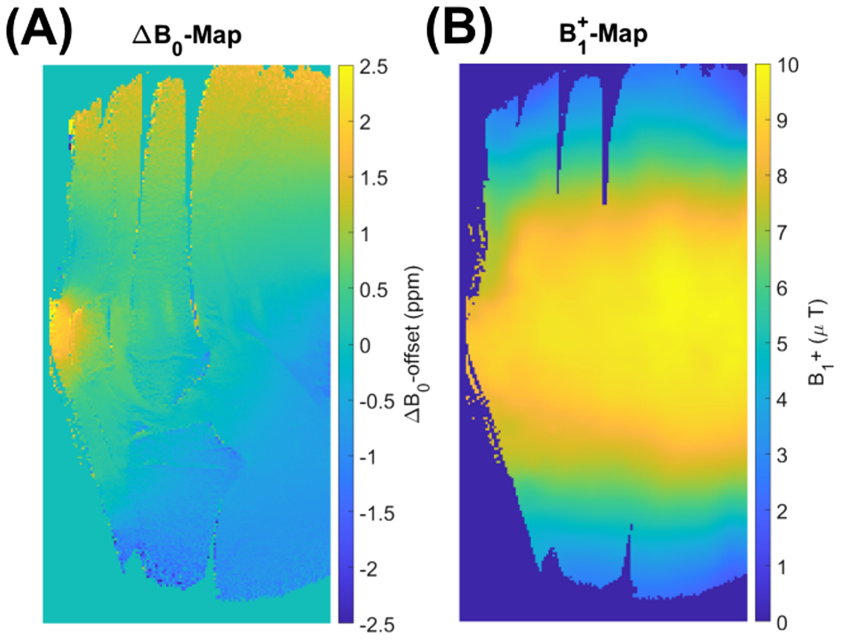

FIGURE 9 Measured ΔB_0 map (A) and measured B_1^+ map of a sagittal slice of the knee (B). The target amplitude is $B_1^+ = 9.46\mu T$ here

time points (Bloch solver plus derivative linearly, time-optimal control loop also linearly); however, speed-up could be achieved by refining the time step iteratively throughout the course of the optimization.[35]

Within the definition of the optimization problem, Equation (6), we demanded a small difference between optimized magnetization and desired magnetization, using a L^p norm. In Equation (7), this constraint was replaced by an L^p norm penalization term. During the course of the

optimization, we started with small $p = 2$ and continued with higher p, always even (to avoid sign issues in the derivatives), to approximate the L^p norm. Together with the iterative choice of α described in subsection 3.1 a perfect inversion over a broad range of variances within ΔB_0 and B_1^+ was observed, but with a slightly higher power integral and hence SAR. If the aim of the optimization is shifted more towards a lower-energy pulse, the reference value S in (11) has to be reduced proportionately.

In contrast to the common approach of using an educated initial guess, the optimization here was started from a random initial RF pulse (i.e., random magnitude and random phase) with a pulse duration of 10ms. The optimal control framework reduced the duration of optim to 3.25ms and yielded an excellent inversion efficiency also for short relaxation times ($T_1 = 102$ms, $T_2 = 81$ms). The amplitude of the optim pulse (yellow line in Figure 1) is almost everywhere on the maximum at 20μT, only the phase (or the frequency) of the pulse varies. During the course of the optimization, it was observed that noticeably better solutions (in the sense of a better inversion efficiency) could be achieved for shorter pulse duration. This coincides with the fact that relaxation affects the inversion efficiency and this behavior increases with an increasing pulse length. Moreover, the optimized pulse optim has superior performance compared with HS1 and HS2 even for longer relaxation times or no relaxation, as shown in Table 1. This suggests that optimization should be done with the set of relaxation times with the smallest values desired, as the efficiency will be as good or better for longer times. To underline this statement, we have carried out an optimization run with the same parameters as chosen to create optim, but with neglected relaxation effects (Figure 10). This resulted in excellent efficiency of more than 94% (which is similar to that of optim); however, when simulating the same RF pulse with relaxation times for white matter the efficiency dropped to 91.3%.

To investigate the influence of the maximum RF amplitude r_{max} on the optimization result, a second optimization run was performed with a lower $r_{max} = 12$μT compared with the $r_{max} = 20$μT default value. The resulting pulse optim low B_1^+ is depicted in Table 2 and Figure 11. The pulse duration remained significantly longer than within the original optim pulse; however, the power integrals of these two pulses are almost identical. The example points out the importance of relaxation for prolonged pulse duration. The simulated inversion efficiency for optim low B_1^+ is inferior with respect to the relaxation times in the phantom and white matter, whereas results without including the relaxation show only a slightly worse performance of optim low B_1^+ compared with optim. This result also underlines the relevance of a time-optimal control formalism if a high efficiency is requested.

We have chosen hyperbolic secant pulses for the comparison in this work due to their use as background suppression pulses in arterial spin labeling[7,28,43] and their excellent robustness to ΔB_0. Using the proposed optimization framework, pulses for the particular background suppression for ASL had already been designed.[46] Therein, the optimized pulse could outperform other hyperbolic secant, WURST and pTx adiabatic pulses.

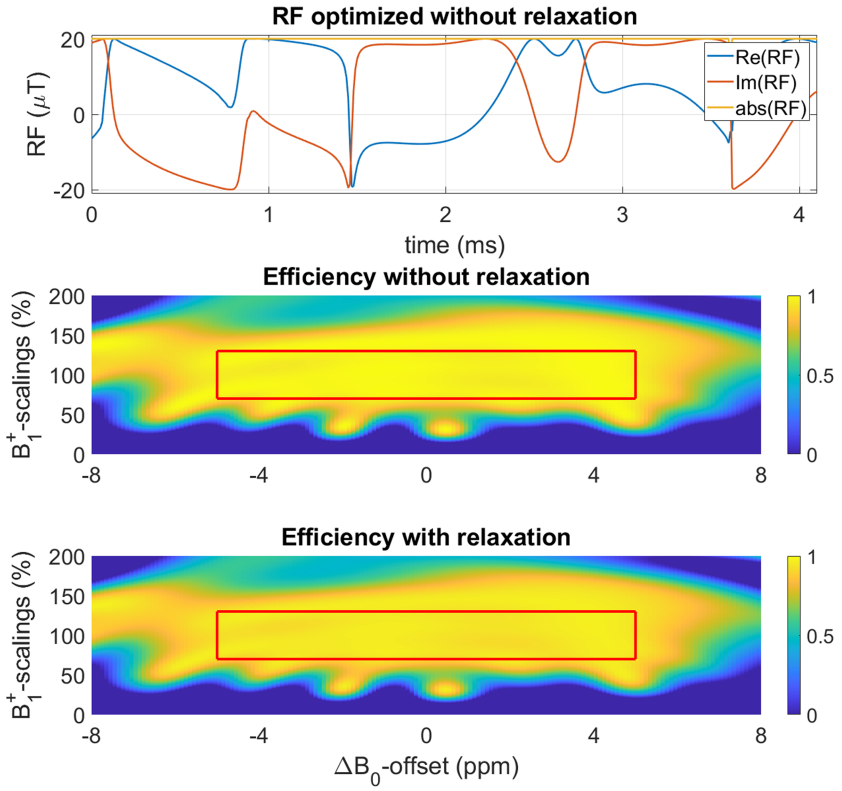

FIGURE 10 Top, RF pulse optimized without accounting for relaxation effects during optimization. Middle, bottom, Efficiency map calculated without relaxation effects (middle) and with relaxation effects corresponding to white matter ($T_1 = 832$ms, $T_2 = 80$ms) (bottom). The red box indicates the area where the optimization was carried out

TABLE 2 Key parameters for an optimized pulse with a lower peak B_1^+ (optim low B_1^+), and a hyperbolic secant pulse of order 8 (HS8)

Pulse	T	Δf	Peak B_1^+	PI	E_{worst}	E_{best}	E_{median}	$90\% - range$	Relaxation
optim low B_1^+	9.82	1.79	12	1.4×10^{-3}	84.19	92.43	89.03	[86.75, 90.50]	phantom
					84.60	93.36	91.25	[88.93, 92.87]	white matter
					90.48	99.99	98.92	[96.09, 99.91]	no relax
HS8	5.00	6.25	20	1.6×10^{-3}	73.37	95.33	92.78	[77.24, 94.99]	phantom
					76.94	97.51	95.87	[80.69, 97.45]	white matter
					78.36	99.96	97.92	[82.17, 99.88]	no relax

Note: The first columns show the pulse duration T in ms, the bandwidth of the pulse Δf in kHz, the peak B_1^+ amplitude in μT and the power integral. The last five columns show the inversion efficiency E as a percentage for the specific set of relaxation times over all combinations of ΔB_0 and B_1^+ included in the optimization of optim, i.e., $\Delta B_0 = \pm 5$ppm and B_1^+ scaled for $\pm 30\%$. We depict the worst case, the best case, the median, and the range where 90% of the efficiencies lie.

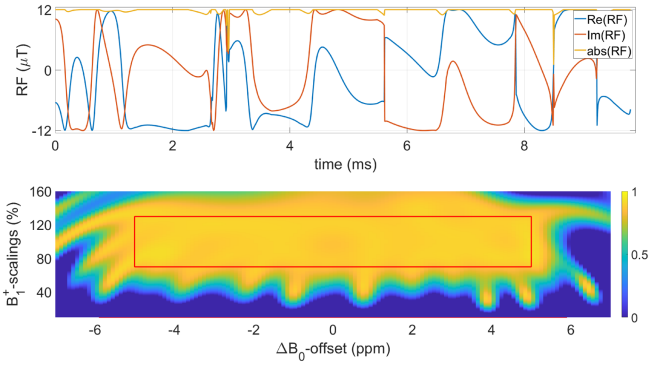

(A) RF pulse (top) and simulated inversion efficiencies (bottom) for a broad range of B_1^+ and ΔB_0 values.

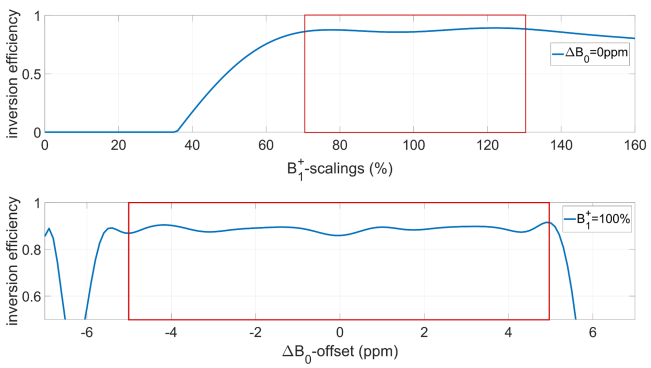

(B) Inversion efficiencies on 2 distinct lines.

FIGURE 11 A, optim low B_1^+ RF pulse (top) and simulated inversion efficiencies (bottom). B_1^+ is scaled from 0% to 160% and ΔB_0 is included for −7ppm to 7ppm at 3 T. B, Simulated inversion efficiencies for a fixed value of $\Delta B_0 = 0$ppm and B_1^+ scaled from 0% to 160% (top) and a fixed B_1^+ scale of 100% and ΔB_0 for −7ppm to 7ppm at 3 T (bottom). The red boxes indicate the areas where the optimization was done

For the comparison made within this paper, HS1 had finally the highest bandwidth of all pulses studied. The reduced inversion efficiency of HS1 can be attributed to the longer pulse duration paired with the short relaxation times. Especially at ultra-high field strengths, this effect will gain importance with decreasing T_2 times in different parenchyma. However, even simulation without relaxation effects shows an efficiency of only 85% for a low B_1^+ (peak amplitude scaled to $\approx 75\%$ of nominal value), reaching an efficiency of 99% and more for B_1^+ scaled to 100% and more. The second hyperbolic secant pulse HS2 was designed with an identical short pulse duration to optim. The inversion efficiency within the defined region of robustness is better than for HS1; however, the significant drawback here is the higher nominal peak amplitude. Therefore, further evaluation on the MR scanner allowed only a scale of 120% of the RF amplitude due to system limits. For the defined target regions it was, however, always possible to find a numerically optimized pulse that achieves in general a higher inversion efficiency than the hyperbolic secant pulses with short pulse duration and no increased B_1^+ amplitude (Figure 1, Table 1). Hyperbolic secant pulses are not limited to a first-order modulation as the presented pulses HS1 and HS2 are. Hyperbolic secant pulses of higher order (e.g. $n = 8$) are typically also of interest and discussed here using HS8 (with parameter $\beta = 530$) (Figure 12 and Table 2). Similarly to HS1, it shows a very evenly distributed performance regarding changes within ΔB_0, paired with a higher inversion efficiency due to the shorter pulse duration. Drawbacks of HS8 are still a less distinct inversion in the lower B_1^+ region and a higher power integral leading to an increased SAR compared with optim.

The phantom measurements on the MR scanner confirmed the simulation results. The accordance between simulation and measurement was excellent for all three RF pulses as seen in Figures 5,6 and 7. For the evaluation of the measurements, the acquired B_1^+ map was used. This allowed the actual B_1^+ amplitude to be taken into account, which deviated considerably from the nominal $B_{1,max}^+$ due to dielectric resonances and coil inhomogeneities. In addition, correcting for relaxation effects as described in Equation (13) brought the reconstructed efficiency as close to the true efficiency as possible.

The additionally optimized pulses optim B_1^+, optim ΔB_0, optim non-robust and optim B_1^+ shift for changed requirements demonstrated the flexibility of proposed optimization framework. For all experiments, the pulse duration could be reduced significantly and the inversion efficiency is (within the target region) better than for optim. Furthermore, the third experiment resulting in optim non-robust demonstrated that reduction

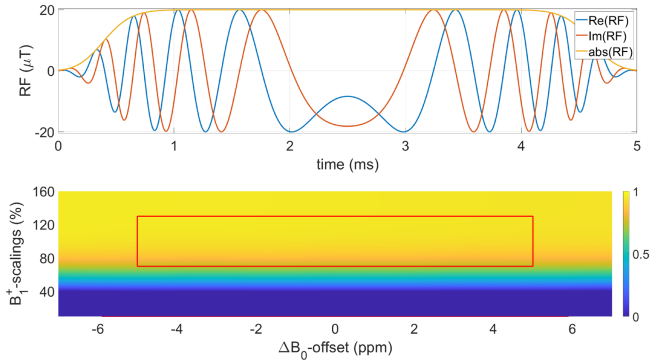

(A) RF pulse (top) and simulated inversion efficiencies (bottom) for a broad range of B_1^+ and ΔB_0 values.

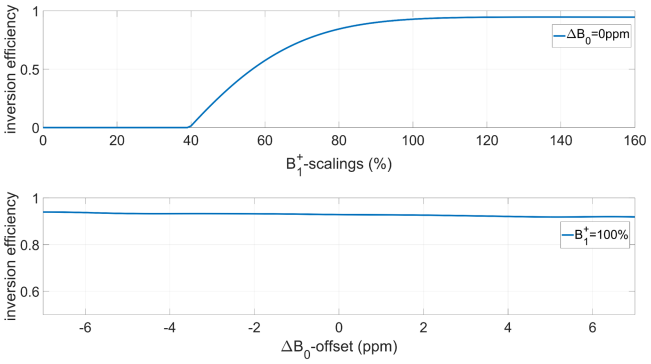

(B) Inversion efficiencies on 2 distinct lines.

FIGURE 12 A, HS8 RF pulse (top) and simulated inversion efficiencies (bottom). B_1^+ is scaled from 0% to 160% and ΔB_0 is included for −7ppm to 7ppm at 3 T. B, Simulated inversion efficiencies for a fixed value of $\Delta B_0 = 0$ppm and B_1^+ scaled from 0% to 160% (top) and a fixed B_1^+ scale of 100% and ΔB_0 for −7ppm to 7ppm at 3 T (bottom)

of pulse energy and the time-optimal formalism work correctly. When calculating the flip angle of this pulse, it turns out to match 180°, indicating equivalence to a simple block pulse. In practice, the decision on which constraints to include in optimization is crucial as it will affect pulse duration and efficiency significantly, as demonstrated. In Figure 4, we saw that for optim B_1^+ and optim B_1^+ shift (plainly B_1^+ robustness for a ΔB_0 offset of 0ppm and 3.4ppm, respectively), some inversion was achieved for B_1^+ at around 65% and ΔB_0 at around ±6.5ppm away from the optimized value. The reason for that is that the effective magnetic field, which causes magnetization to tip, is coincidentally around the same here as for the optimized area. Interestingly, the same behavior can be observed for 90_x–180_y–90_x composite RF pulses, which provide B_1^+ but no ΔB_0 robustness.[16]

During the measurement of the subject's knee, we demonstrated the usability of the optimized pulse for in vivo applications. The setup (i.e., knee coil, sagittal acquisition) was chosen to include natural ΔB_0 and continuous B_1^+ field changes. In Figure 9 the B_1^+ map revealed a severe loss towards the proximal and distal directions of the knee, whilst in Figure 8 optim has been proven to have the best performance in these directions. The ΔB_0 map in Figure 9 revealed changes within the B_0 field for up to ±2.5ppm in addition to fat–water shift (bone marrow–muscle).

The applications of the inversion pulses studied are diverse, as described earlier.[1–11] Compared with methods that try to improve the field inhomogeneities by technical measures (e.g., B_1 shimming using parallel transmit or dynamic B_0 shimming in the abdomen), the use of robust pulses is much simpler, easy to integrate into existing sequences and inexpensive. The developed framework can be further adapted for other issues such as layer-selective refocusing pulses.

6 | CONCLUSION

We have introduced a novel optimal control framework for ΔB_0- and B_1^+-robust, and time-optimal RF pulse design. The flexibility and robustness of the optimization framework were demonstrated using a random RF pulse as an initial guess, and aiming for varying optimization targets. Compared with two adiabatic, hyperbolic secant pulses, a superior performance in terms of inversion efficiency, pulse duration and peak amplitude could be demonstrated in phantom and in vivo measurements. The proposed framework is flexible, and parameters can be adapted easily to other requirements, such as different field strengths.

FINANCIAL DISCLOSURE

None reported.

CONFLICT OF INTEREST

The authors declare no potential conflict of interests.

ORCID

Christina Graf https://orcid.org/0000-0001-7248-1569
Martin Soellradl https://orcid.org/0000-0002-3760-5578
Christoph Stefan Aigner https://orcid.org/0000-0003-3618-9610

Armin Rund https://orcid.org/0000-0001-7934-4970
Rudolf Stollberger https://orcid.org/0000-0002-4969-3878

REFERENCES

1. Hajnal JV, De Coene B, Lewis PD, et al. High signal regions in normal white matter shown by heavily T2-weighted CSF nulled IR sequences. *J Comput Assist Tomogr*. 1992;16:506-513.
2. Redpath TW, Smith FW. Use of a double inversion recovery sequence to image selectively grey or white brain matter. *Br J Radiol*. 1994;67(804):1258-1263.
3. Young IR, Hall AS, Bydder GM. The design of a multiple inversion recovery sequence for T1 measurement. *Magn Reson Med*. 1987;5:99-108.
4. Bydder GM, Young IR. MR imaging: clinical use of the inversion recovery sequence. *J Comput Assist Tomogr*. 1985;9:659-675.
5. Cudalbu C, Behar KL, Bhattacharyya PK, et al. Contribution of macromolecules to brain ^{1}H MR spectra: experts' consensus recommendations. *NMR Biomed*. 2021;e4393:34.
6. Alsop DC, Detre JA, Golay X, et al. Recommended implementation of arterial spin-labeled perfusion MRI for clinical applications: a consensus of the ISMRM Perfusion Study Group and the European Consortium for ASL in Dementia. *Magn Reson Med*. 2014;73:102-116.
7. Garcia DM, Duhamel G, Alsop DC. Efficiency of inversion pulses for background suppressed arterial spin labeling. *Magn Reson Med*. 2005;54:366-372.
8. Kellmann P, Herzka DA, Schacht Hansen M. Adiabatic inversion pulses for myocardial T1 mapping. *Magn Reson Med*. 2014;71:1428-1432.
9. Aherne E, Chow K, Carr J. Cardiac T1 mapping: techniques and applications. *J Magn Reson Imaging*. 2020;51:1336-1356.
10. Cooper MA, Nguyen TD, Spincemaille P, Prince MR, Weinsaft JW, Wang Y. How accurate is MOLLI T1 mapping in vivo? Validation by spin echo methods. *PLoS ONE*; 9(9):e107327.
11. Rodgers CT, Piechnik SK, DelaBarre LJ, et al. Inversion recovery at 7 Tesla in the human myocardium: measurement of T_1, inversion efficiency and B_1^+. *Magn Reson Med*. 2013;70(4):1038-1046.
12. de Graaf RA. *In Vivo NMR Spectroscopy*: Wiley; 2007.
13. Bernstein MA, King KF, Zhou XJ. *Handbook of MRI Pulse Sequences*: Elsevier; 2004.
14. Moore J, Jankiewicz M, Zeng H, Anderson AW, Gore JC. Composite RF pulses for B_1^+-insensitive volume excitation at 7 Tesla. *J Magn Reson*. 2010;205:50-62.
15. Garwood M, Ke Y. Symmetric pulses to induce arbitrary flip angles with compensation for rf inhomogeneity and resonance offsets. *J Magn Reson*. 1991;94:511-525.
16. Lurie DJ. Numerical design of composite radiofrequency pulses. *J Magn Reson*. 1986;70:11-20.
17. Johnson AJ, Garwood M, Ugurbil K. Slice selection with gradient-modulated adiabatic excitation despite the presence of large B_1 inhomogeneities. *J Magn Reson*. 1989;81:653-660.
18. Warnking JM, Pike GB. Bandwidth-modulated adiabatic RF pulses for uniform selective saturation and inversion. *Magn Reson Med*. 2004;52:1190-1199.
19. MacLennan T, Seres P, Rickard J, Stolz E, Beaulieu C, Wilman AH. Characterization of B_1^+ field variation in brain at 3 T using 385 healthy individuals across the lifespan. *Magn Reson Med*. 2022;87:960-971.
20. Schär M, Vonken EJ, Stuber M. Simultaneous B_0- and B_1^+-map acquisition for fast localized shim, frequency and RF power determination in the heart at 3 T. *Magn Reson Med*. 2010;63(2):419-426.
21. Lesch A, Schloegl M, Holler M, Bredies K, Stollberger R. Ultrafast 3D Bloch–Siegert B_1^+-mapping using variational modeling. *Magn Reson Med*. 2019;81:881-892.
22. Kraff O, Quick HH. Radiofrequency coils for 7 Tesla MRI. *Top Magn Reson Imaging*. 2019;28(3):145-158.
23. Hurley AC, Al'Radaideh A, Bai L, Aickelin U, Coxon R, Glover P, Gowland PA. Tailored RF pulse for magnetization inversion at ultrahigh field. *Magn Reson Med*. 2010;63:51-58.
24. Deichmann R, Good CD, Josephs O, Ashburner J, Turner R. Optimization of 3-D MP-RAGE sequences for structural brain imaging. *NeuroImage*. 2000;12:112-127.
25. Kobzar K, Skinner TE, Khaneja N, Glaser SJ, Luy B. Exploring the limits of broadband excitation and inversion: II. RF-power optimized pulses. *J Magn Reson*. 2008;194:58-66.
26. Hajnal JV, Oatridge A, Herlihy AH, Bydder GM. Reduction of CSF artifacts on FLAIR images by using adiabatic inversion pulses. *Am J Neuroradiol*. 2001;22:317-322.
27. Wang J, Mao W, Quin M, Smith MB, Constable RT. Factors influencing flip angle mapping in MRI: pulse shape, slice-select gradients, off-resonance excitation, and B0 inhomogeneities. *Magn Reson Med*. 2006;56:463-468.
28. Wang K, Shao X, Yan L, Ma SJ, Jin J, Wang D. Optimization of adiabatic pulses for pulsed arterial spin labeling at 7 Tesla: comparison with pseudo-continuous arterial spin labeling. *Magn Reson Med*. 2021;6:3277-3240.
29. Herlihy AH, Oatridge A, Curati WL, Puri BK, Bydder GM, Hajnal JV. FLAIR imaging using nonselective inversion pulses combined with slice excitation order cycling and k-space reordering to reduce flow artifacts. *Magn Reson Med*. 2001;46:354-364.
30. Conolly S, Nishimura D, Macovski A. Optimal control solutions to the magnetic resonance selective excitation problem. *IEEE Trans Med Imaging*. 1986;5:106-115.
31. Xu D, King KF, Zhu Y, McKinnon GC, Liang Z. Designing multichannel, multidimensional, arbitrary flip angle RF pulses using an optimal control approach. *Magn Reson Med*. 2008;59:547-560.
32. Grissom WA, Xu D, Kerr AB, Fessler JA, Noll DC. Fast large-tip-angle multidimensional and parallel RF pulse design in MRI. *IEEE Trans Med Imaging*. 2009;28:1548-1559.
33. Aigner CS, Clason C, Rund A, Stollberger R. Efficient high-resolution RF pulse design applied to simultaneous-multislice excitation. *J Magn Reson*. 2016;263:33-44.
34. Rund A, Aigner CS, Kunisch K, Stollberger R. Magnetic resonance RF pulse design by optimal control with physical constraints. *IEEE Trans Med Imaging*. 2018;37:461-472.
35. Rund A, Aigner CS, Kunisch K, Stollberger R. Simultaneous multislice refocusing via time optimal control. *Magn Reson Med*. 2018;80:1416-1428.

36. Aigner CS, Rund A, Abo Seada S, et al. Time optimal control-based rf pulse design under gradient imperfections. *Magn Reson Med*. 2020;2:561-574.
37. Rosenfeld D, Zur Y. Design of adiabatic selective pulses using optimal control theory. *Magn Reson Med*. 1996;36(3):401-409.
38. Van Reeth E, Ratiney H, Tesch M, Grenier D, Beuf O, Glaser SJ, Sugny D. Optimal control design of preparation pulses for contrast optimization in MRI. *J Magn Reson*. 2017;279:39-50.
39. Van Reeth E, Ratiney H, Beuf O, Kanice S, Glaser SJ, Sugny D. BEEEP: B1-robust energy efficient excitation pulses. In: ISMRM 27th Annual Meeting and Exhibition; May 11-16, 2019; Montreal, Canada; 2019.
40. Graf C, Rund A, Aigner CS, Stollberger R. Accuracy and performance analysis for Bloch and Bloch–McConnell simulation methods. *J Magn Reson*. 2021;326:107011. doi:10.1016/j.jmr.2021.107011
41. Tröltzsch F. Optimal Control of Partial Differential Equations. Vieweg + Teubner; 2009.
42. Mannel F, Rund A. A hybrid semismooth quasi-Newton method for nonsmooth optimal control with PDEs. *Optim Eng*. 2020;22:2087-2125.
43. Vidoretta M, Wang Z, Rodriguez I, Pastor MA, Detre JA, Fernandez-Seara MA. Comparison of 2D and 3D single-shot ASL perfusion fMRI sequences. *NeuroImage*. 2013:662-671.
44. Wansapura J, Holland S, Scott DR, Ball W. NMR relaxation times in the human brain at 3.0 Tesla. *J Magn Reson Imaging*. 1999;9:531-538.
45. Sacolick LI, Wiesinger F, Hancu I, Vogel MW. B_1 mapping by Bloch–Siegert shift. *Magn Reson Med*. 2010;63:1315-1322.
46. Zhao C, Wang K, Graf C, Stollberger R, Wang DJJ. Optimization and evaluation of inversion pulses for background suppressed pseudo-continuous arterial spin labeling at 7T. In: Joint Annual Meeting ISMRM–ESMRMB; May 7–12, 2022; London, UK; 2022.

How to cite this article: Graf C, Soellradl M, Aigner CS, Rund A, Stollberger R. Advanced design of MRI inversion pulses for inhomogeneous field conditions by optimal control. *NMR in Biomedicine*. 2022;35(11):e4790. doi:10.1002/nbm.4790